catalysts

MDPI

Article

Effect of Ce Content on the Chemical Looping Oxidative Dehydrogenation of Propane to Propylene over a VO_x-CeO_2/γ-Al_2O_3 Oxygen Carrier

Fangyuan Qiang [1], Tuo Guo [2], Mengdong Nie [1], Yongzhuo Liu [1], Man Wu [1,*] and Qingjie Guo [1,2,*]

[1] College of Chemical Engineering, Qingdao University of Science & Technology, Qingdao 266042, China; fyqiang@mails.qust.edu.cn (F.Q.); yzliu@qust.edu.cn (Y.L.)
[2] State Key Laboratory of High-Efficiency Coal Utilization and Green Chemical Engineering, College of Chemistry and Chemical Engineering, Ningxia University, Yinchuan 750021, China
* Correspondence: wuman@qust.edu.cn (M.W.); qjguo@qust.edu.cn (Q.G.)

Abstract: The chemical looping oxidative dehydrogenation of propane to propylene (CL-ODHP) replaces molecular oxygen with lattice oxygen (O_{latt}) in oxygen carriers. This method boosts propylene selectivity by avoiding the deep oxidation of propane. Herein, a series of 10V-XCe/Al oxygen carriers with different Ce contents were prepared to realize different VO_x-CeO_y interactions. The effect of the Ce content in 10V-XCe/Al oxygen carriers on the CL-ODHP reaction was studied and the optimal Ce content was determined. CeO_2 prevents the outward diffusion and evolution of O_{latt} in VO_x carriers to the adsorbed electrophilic oxygen species (O_{elec}), effectively inhibiting the loss of O_{latt}, improving the selectivity of propylene, and extending the lifetime and activity of the oxygen carriers. After characterizing and analyzing the oxygen carriers, it was found that 10V-3Ce/Al has the highest specific surface area, highest oxygen capacity, and lowest reducibility. The 10V-3Ce/Al also delivers the highest oxidative dehydrogenation performance. At 550 °C, the average propylene and CO_x selectivity values of 10V-3Ce/Al were 81.87% and 7.28%, respectively (vs. 62.79% and 25.64% respectively, for 10V/Al). It is demonstrated that 10V-3Ce/Al exhibits good cycle stability with no significant decrease in catalytic performance after 15 cycles. In situ diffuse-reflectance infrared Fourier-transform spectroscopy indicates that CL-ODHP on 10V-3Ce/Al undergoes the Mars-van Krevelen mechanism. The migration and evolution of O_{latt} in oxygen carriers is controlled by reasonably modifying the metal oxide interactions to improve propylene yield. This work will thus guide the subsequent development of novel and efficient CL-ODHP oxygen carriers.

Keywords: propane dehydrogenation; vanadium oxide; chemical looping; lattice oxygen

Citation: Qiang, F.; Guo, T.; Nie, M.; Liu, Y.; Wu, M.; Guo, Q. Effect of Ce Content on the Chemical Looping Oxidative Dehydrogenation of Propane to Propylene over a VO_x-CeO_2/γ-Al_2O_3 Oxygen Carrier. *Catalysts* **2023**, *13*, 797. https://doi.org/10.3390/catal13050797

Academic Editor: Maurizio Muniz-Miranda

Received: 28 March 2023
Revised: 19 April 2023
Accepted: 23 April 2023
Published: 24 April 2023

1. Introduction

Propylene is an important raw material for petrochemicals, and is mainly used to produce chemical materials such as polypropylene, propylene oxide, and acrylonitrile. The demand for propylene has increased with development in the downstream market. The current development in the shale gas industry has increased the availability of low-cost propane, making propylene production from propane appealing [1,2].

The industrial process, direct dehydrogenation of propane to propylene (DHP), is a strong heat-absorption process with restricted thermodynamic equilibrium. Effective propane conversion requires a high temperature, which increases the risk of problems such as catalyst carbon build-up. These inherent drawbacks limit the performance of catalytic dehydrogenation of propane [3,4]. In contrast, oxidative dehydrogenation of propane to propylene (ODHP) is an exothermic reaction not limited by thermodynamics. As ODHP can theoretically achieve high conversion rates at lower temperatures than DHP without carbon accumulation, it has attracted extensive research interest. However, in this process, O_2 deeply oxidizes propane to CO_x, which reduces propylene production. The widespread

adoption of ODHP is further limited by the requirement for expensive air-separation equipment. The safety of co-feeding propane and O_2 raises additional concerns [5,6].

The shortcomings of propylene production technologies can be overcome by a new propylene production route called chemical looping oxidative dehydrogenation of propane to propylene (CL-ODHP), which includes oxidation and reduction reactions using oxygen carriers in two reactors. Propane is oxidized to propylene and water by lattice oxygens (O_{latt}) in the oxygen carrier. The water is separated from the reaction system via condensation, driving the reaction equilibrium in the positive direction and thus increasing the propylene yield. The reduced oxygen carrier enters the air reactor, where it is oxidized and regenerated before entering the dehydrogenation reactor to complete the oxidation and dehydrogenation cycles [7,8]. The CL-ODHP process confers the following advantages over other propylene production processes: (a) the oxygen carrier avoids direct contact between propane and O_2, thereby eliminating explosion risks; (b) the process does not require an air separation device, reducing the investment and operating costs; (c) the reaction occurs without O_2, improving the operability and temperature control; and (d) hydrogen combustion is indirect and flameless, thus reducing CO_x emissions.

However, the CL-ODHP process requires suitable oxygen carriers. Metal oxides have been reported as suitable oxygen carriers for chemical looping processes. Liu et al. [9] found that polymetallic oxide oxygen carriers have high CL-ODHP activity, and by regulating the ratio between metal oxides, the polymetallic oxide oxygen carriers can be made to release O_{latt} slowly, thus improving the selectivity of low-carbon olefins. After studying the CL-ODHP properties of different metal oxides (MoO_x/γ-Al_2O_3, GaO_x/γ-Al_2O_3, and VO_x/γ-Al_2O_3) as oxygen carriers, Wu et al. [10] found that VO_x/γ-Al_2O_3 oxygen carriers can conduct CL-ODHP reactions at a lower temperature and have higher CL-ODHP activity. Although VO_x/γ-Al_2O_3 has subsequently attracted wide research interest, Jiang et al. [11] found that O_{latt} in VO_x/γ-Al_2O_3 oxygen carriers are rapidly released and propane is deeply oxidized to CO_x, causing propylene selectivity to deteriorate. This selectivity can be improved by a metal-oxide promoter that regulates the O_{latt} release rate of the VO_x/γ-Al_2O_3 oxygen carrier. According to previous research, CeO_2 has excellent oxygen storage and release characteristics as well as redox properties, which can change the O_{latt}-transfer ability of adjacent metal oxides [12,13]. Hedun et al. [14] prepared $FeCeO_x$ as an oxygen carrier via the impregnation method. They reported that CeO_2 inhibits the conversion rate of O_{latt} to O_{elec} in Fe-based oxygen carriers, thereby improving propylene selectivity. To similarly regulate the slow release of O_{latt} and improve propylene selectivity, we add CeO_2 to VO_x/γ-Al_2O_3 oxygen carriers and investigate the synergistic effect of VO_x and CeO_2 oxygen carriers on the CL-ODHP reaction. We also add bimetallic oxides to improve propylene selectivity. CeO_2 increases the oxygen capacity of the carrier and controls the O_{latt}-release rate in the VO_x/γ-Al_2O_3 oxygen carrier. To determine the optimum Ce content for increasing the propylene yield, we prepared a series of VO_x (10 wt.%)-CeO_2 (X wt.%)/γ-Al_2O_3 oxygen carriers (X = 0, 1, 3, 5, 7) for the CL-ODHP reaction and investigated the effect of Ce content on the physicochemical properties of the oxygen carriers. These properties were then related to the reactivity performance of CL-ODHP.

2. Oxygen Carrier Characterization

2.1. XRD Characterization Results

Figure 1 shows XRD profiles of the fresh 10V/Al, 10V-1Ce/Al, 10V-3Ce/Al, 10V-5Ce/Al, and 10V-7Ce/Al oxygen carriers. The diffraction peaks at 2θ = 45.56° and 67.03° are assigned to mesoporous γ-Al_2O_3 (JCPDS 10-0425) [15]. With increasing Ce content in the oxygen carrier, the peak intensity corresponding to the CeO_2 phase becomes sharper and more intense. The diffraction peaks at 2θ = 28.89°, 32.38°, and 47.85° characterize the cubic crystal structure of the CeO_2 phase, indicating that CeO_2 exists in the cubic fluorite phase. The diffraction peaks of VO_x species are absent, possibly because these species are highly dispersed on the surface of the γ-Al_2O_3 carrier, rendering them undetectable by the XRD instruments [16].

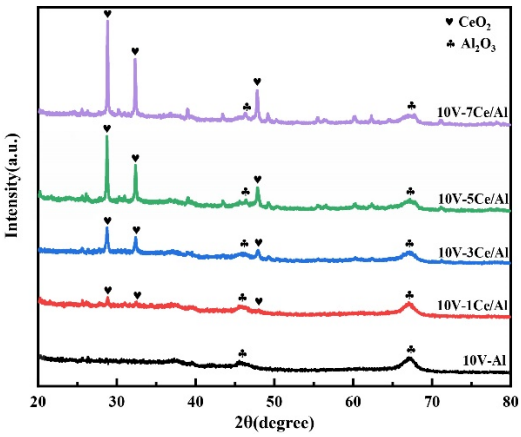

Figure 1. XRD spectra of the 10V-XCe/Al oxygen carriers (X = 0, 1, 3, 5, 7).

2.2. Analysis of Oxygen Carrier Morphology

Figure 2a–d shows the morphological characteristics of the oxygen carriers detected via SEM. All oxygen carriers appear as spherical particles with numerous surface folds. The surface smoothness of the 10V-XCe/Al oxygen carriers increases with increasing Ce content from 0 to 3 wt.%. When the Ce content reaches 7 wt.% (10V-7Ce/Al), the surface is rendered uneven by particle agglomeration.

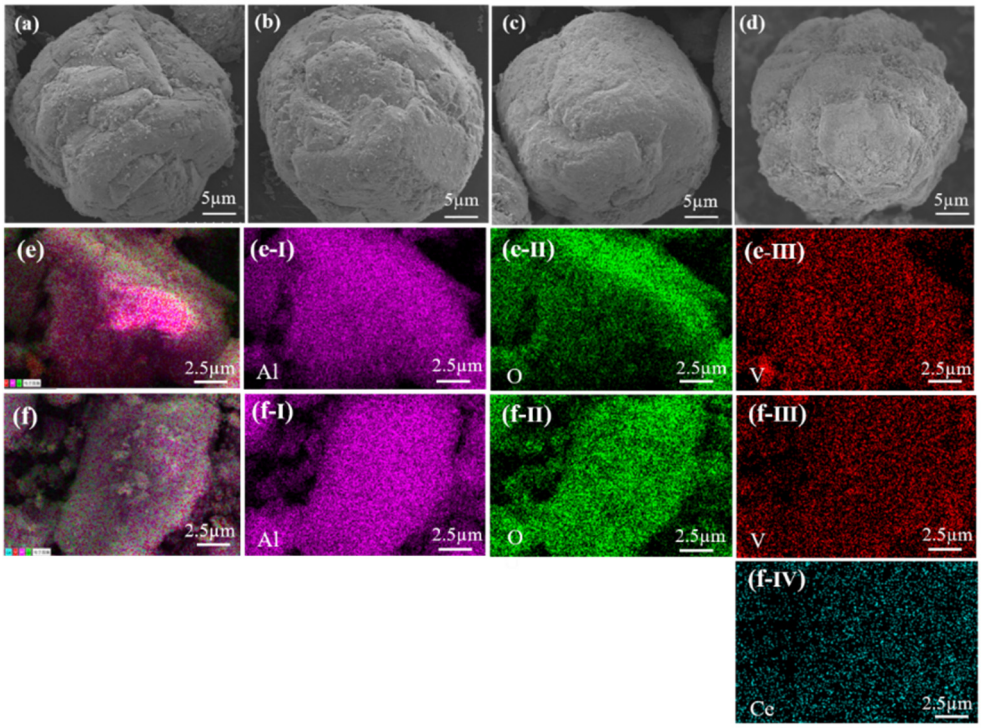

Figure 2. SEM images of (**a**) 10V/Al, (**b**) 10V-1Ce/Al, (**c**) 10V-3Ce/Al, and (**d**) 10V-7Ce/Al; elemental maps of (**e**) 10V/Al and (**f**) 10V-3Ce/Al (**I**: aluminum; **II**: oxygen; **III**: vanadium; **IV**: cerium).

The distributions of the Al, V, O, and Ce elements were investigated through mapping energy spectral analysis. Figure 2e,f shows the mapping images of the 10V/Al and 10V-3Ce/Al oxygen carriers, respectively. Each metal can be distinguished in the maps. Comparison of Figure 2e-III and Figure 2f-III shows that Ce introduction improves the uniformity of the V species through the sample. Moreover, Figure 2(e-II,f-II) shows that the introduction of Ce resulted in a denser distribution of O species through the samples,

indicating that Ce increases the O content. As shown in Figure 2(f-IV), the Ce species is uniformly distributed on the surface of 10V-3Ce/Al.

Figure 3 shows the TEM of a fresh 10V-3Ce/Al oxygen carrier, where the polycrystalline material consists of small randomly oriented crystal structure domains. The lattice stripe spacing d = 0.31 nm and 0.26 nm correspond to the (111) crystal plane and the (200) crystal plane of CeO_2, respectively [17]. The lattice stripe spacing d = 0.28 nm corresponds to the (301) crystal planes of V_2O_5 [18]. By Figures 2 and 3, it is shown that CeO_2 and V_2O_5 are uniformly dispersed on the surface of the oxygen carrier.

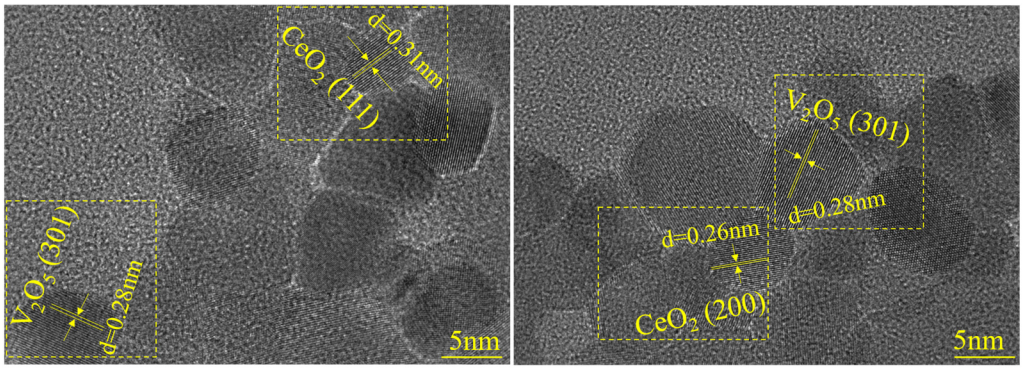

Figure 3. TEM images of 10V-3Ce/Al oxygen carrier.

2.3. Pore-Structure Analysis of the Oxygen Carriers

Figure 4 shows the isothermal sorption and desorption curves of the oxygen carriers. The sorption and desorption curves of γ-Al_2O_3 and all oxygen carriers are type IV and exhibit H4-type hysteresis loops with low-pressure adsorption (P/P_0 = 0–0.10, where P and P_0 denote that P is the true pressure of the gas and P_0 is the saturated vapor pressure of the gas at the measured temperature, respectively), indicating that the oxygen carriers contain few micropores. When P/P_0 = 0.40, capillary coalescence occurs, resulting in a rapid increase in the adsorption amount [19].

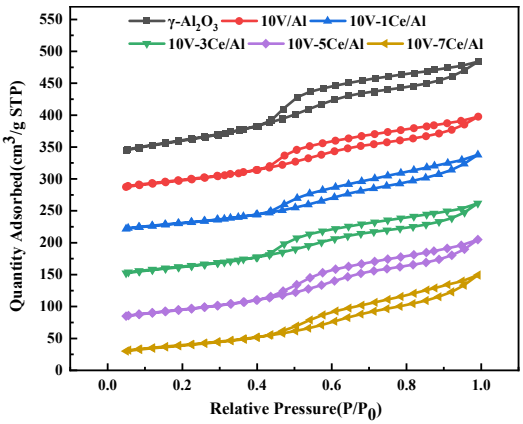

Figure 4. N_2 adsorption-desorption isotherms of γ-Al_2O_3 and the 10V-XCe/Al oxygen carriers.

Table 1 summarizes the pore-structure parameters of the oxygen carriers. γ-Al_2O_3 exhibits the highest specific surface area (206.87 m^2/g), implying that it enhances the oxygen carrier's performance most favorably. The specific surface area decreases to 119.95 m^2/g after impregnating the VO_x species. In the 10V-XCe/Al oxygen carriers, the pore structure parameters first increase and then decrease with increasing Ce content. The specific surface area, pore volume, and pore diameter are maximized in 10V-3Ce/Al (131.10 m^2/g, 0.21 cm^3/g, and 5.38 nm, respectively). These results indicate that adding a small amount of Ce to the 10V/Al oxygen carrier increases the specific surface area of the oxygen carrier,

allowing more uniform dispersion of the active component on the carrier surface. Further, the enlarged pore size benefits propylene desorption [20].

Table 1. Structural properties of γ-Al_2O_3 and the 10V-XCe/Al oxygen carriers.

Samples	S_{BET} (m^2/g)	V_p (cm^3/g)	D_p (nm)
γ-Al_2O_3	206.87	0.25	3.25
10V-Al	119.95	0.18	4.64
10V-1Ce/Al	124.91	0.19	4.95
10V-3Ce/Al	131.10	0.21	5.38
10V-5Ce/Al	104.29	0.16	4.30
10V-7Ce/Al	90.13	0.11	3.75

2.4. Thermal Stabilities of the Oxygen Carriers

Figure 5 plots the TGA and differential thermogravimetric (DTG) curves of the 10V-XCe/Al samples (X = 0, 1, 3, 5, 7) as the temperature was increased from 50 °C to 800 °C in inert nitrogen gas. The DTG curves (Figure 5b) present a weight-loss peak at 90–120 °C, which probably represents the evaporation of physical water molecules from the sample surfaces [21]. The oxygen carrier with the highest cerium content (7 Ce) shows the least weight loss (Figure 5). The thermal stability of the oxygen carriers increases with increasing Ce loading, probably because the CeO_2 phase inhibits γ-Al_2O_3 sintering and phase transition at high temperatures [22].

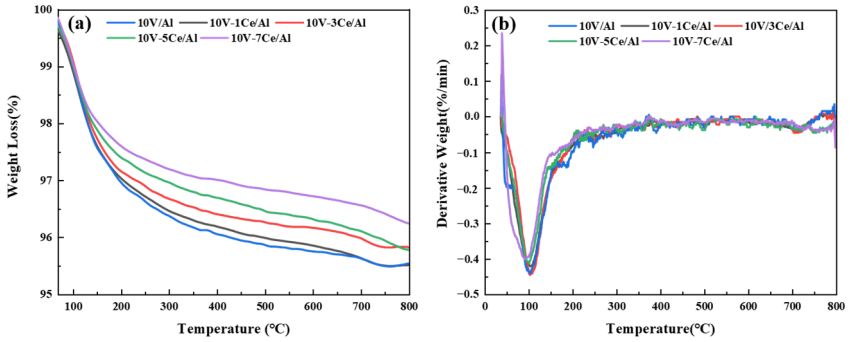

Figure 5. (**a**) Thermogravimetric and (**b**) differential thermogravimetric curves of the oxygen carriers.

2.5. Reduction Properties of the Oxygen Carriers

The reducibility and oxygen-carrying capacities of the oxygen carriers were characterized using H_2-TPR. The H_2-TPR curves of all oxygen carriers are shown in Figure 6a. The 3Ce/Al oxygen carrier shows a reduction peak near 450 °C, which is attributed to the reduction of Ce^{4+}, and the reduction peak of CeO_2 phase overlaps with the reduction peak of VO_x species [23]. The 10V/Al oxygen carrier shows an initial large reduction peak near 450 °C, attributed to the reduction of amorphous monomer or polymeric VO_x species phases with oxidation states between V^{5+} and V^{4+} [24]. Therefore, in the temperature range of 400-550 °C, the H_2 absorption is equal to the sum of H_2 consumed during the reduction of the VO_x phase and the CeO_2 phase. Increasing the Ce loading increasingly shifts the position of the reduction peak from that of 10V/Al. Therefore, CeO_2 changes the reducibility of the oxygen carrier. Moreover, the reducibility decreases gradually with temperature from left to right and its strength decreases in the order of 10V/Al > 10V-7Ce/Al > 10V-5Ce/Al > 10V-1Ce/Al > 10V-3Ce/Al. Gu [25] and Leon [26], who investigated the relationship between oxygen carrier reducibility and propylene selectivity, reported that lower reducibility usually corresponds to higher propylene selectivity.

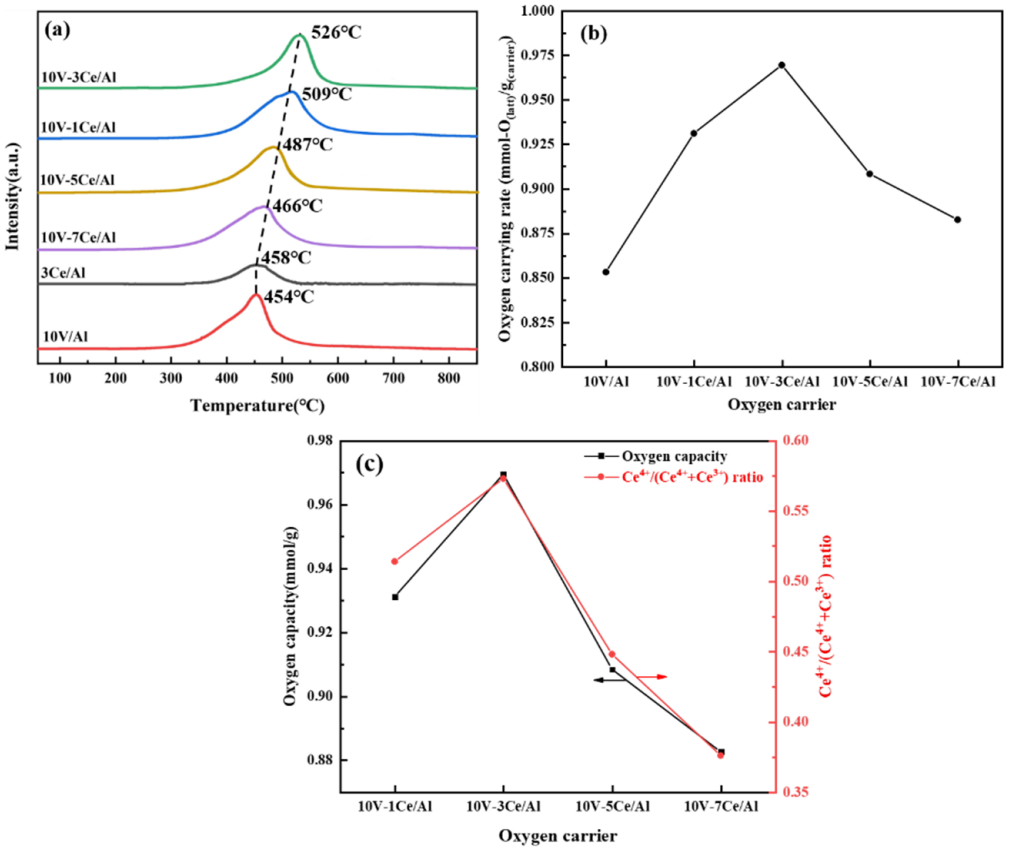

Figure 6. (**a**) H_2-temperature programmed reduction spectra and (**b**) oxygen carrying capacities of the oxygen carriers; (**c**) ratios of Ce^{4+} content to (Ce^{4+} + Ce^{3+}) content and oxygen carrying capacities in the oxygen carriers with different Ce contents.

The oxygen loadings in the oxygen carriers were calculated from the hydrogen consumptions of the carriers. Although the oxygen carrier conducts the H_2-reduction process on its surface, the consumed O_{latt} is supplied from its interior [24]. As shown in Figure 6b, increasing the Ce content does not monotonically increase the amount of O_{latt} stored in the carrier; the oxygen loading is maximized in the carrier containing 3 wt.% Ce.

2.6. XPS Elemental Valence Analysis of the Oxygen Carriers

Figure 7a shows the Ce 3d XPS spectra of the oxygen carriers. Due to the splitting of the Ce $3d_{3/2}$ and Ce $3d_{5/2}$ main peaks and the different final states after relaxation, the XPS spectra of Ce species can be deconvoluted into six peaks. Peaks at 904.03 and 885.22 eV were attributed to Ce^{3+}, and peaks at 907.04, 900.72, 898.17, and 881.74 eV were attributed to Ce^{4+} [27]. The Ce^{4+} species improve the electron-transfer channel and optimize the activity of the oxygen-carrier O_{latt}, thereby facilitating the dehydrogenation reaction [17]. Increasing the Ce loading in the oxygen carrier increases the total area of the Ce 3d peak. The Ce^{4+} to (Ce^{4+} + Ce^{3+}) ratio is largest (57.32%) in 10V-3Ce/Al whereas the percentage of Ce^{4+} is smallest (37.64%) in 10V-7Ce/Al. The change in $Ce^{4+}/(Ce^{4+} + Ce^{3+})$ ratio follows the oxygen-loading trend of the oxygen carriers (Figure 6c). However, O_{latt} is present only in CeO_2 and is absent in Ce^{3+} species [28]. When the mass fraction of Ce content in the oxygen carrier exceeds 3 wt.%, the Ce^{3+} content increases while the Ce^{4+} content decreases.

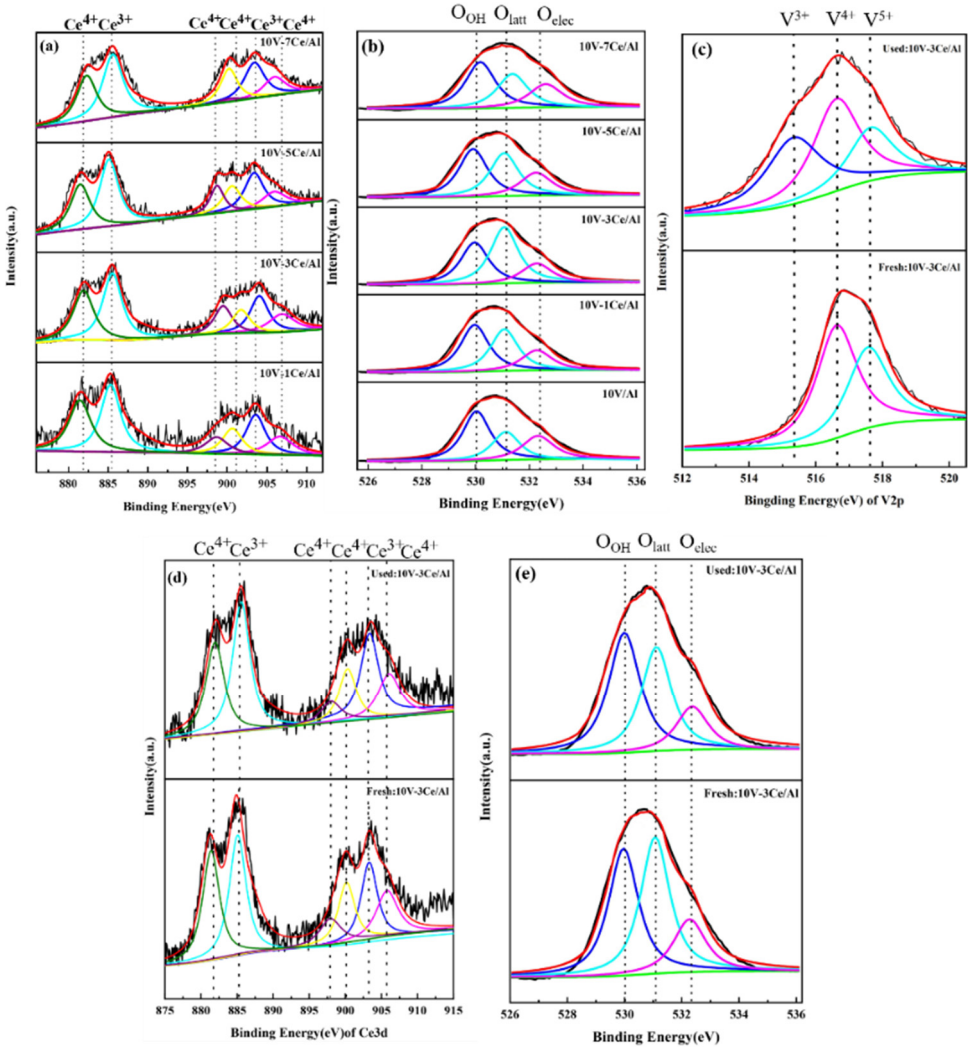

Figure 7. (**a**) Ce 3d XPS spectra and (**b**) O 1s XPS spectra of the oxygen carriers; (**c**) V 2p XPS spectra, (**d**) Ce 3d XPS spectra, and (**e**) O1s XPS spectra before and after the 10V-3Ce/Al reaction.

Figure 7b shows the XPS pattern of O 1s of fresh oxygen carriers, the peak at 530.02 eV corresponds to the adsorbed hydroxyl oxygen species (O_{OH}), the peak at 531.17 eV corresponds to the lattice oxygen species (O_{latt}), and the peak at 532.39 eV corresponds to the electrophilic oxygen species (O_{elec}) [29]. As shown in Table 2, the content of the oxygen carrier O_{latt} increases significantly with increasing Ce loading, reaching a maximum of 10V-3Ce/Al. More O_{latt} promotes the selective oxidation of propane to propylene, thus improving propylene selectivity. The content of O_{elec} decreases with increasing Ce loading, and the highest concentration of Ce^{4+} is found in 10V-3Ce/Al oxygen carriers, where Ce^{4+} inhibits the conversion of O_{latt} to O_{elec} on the surface of the oxygen carriers, thus storing more O_{latt} for the carriers [27]. Figure 7e shows the O 1s XPS spectra before and after the reaction of 10V-3Ce/Al oxygenates, and the O_{latt} content of the oxygenate decreased significantly after the reaction. However, the rate of conversion of O_{latt} to O_{elec} was inhibited by the presence of Ce^{4+}, and the oxidative dehydrogenation of propane also consumed O_{elec}, so the content of O_{elec} decreased after the reaction.

Table 2. Relative content of oxygen species on the surface of fresh oxygen carriers.

Oxygen Carrier	$O_{latt}/(O_{OH} + O_{latt} + O_{elec})$	$O_{elec}/(O_{OH} + O_{latt} + O_{elec})$
10V/Al	31.45%	27.78%
10V-1Ce/Al	37.63%	22.01%
10V-3Ce/Al	45.38%	19.03%
10V-5Ce/Al	35.61%	23.51%
10V-7Ce/Al	33.77%	26.08%

Figure 7c compares the XPS spectra of V 2p before and after the 10V-3Ce/Al reaction. The peaks at 515.35, 516.65, and 517.64 eV belong to V^{3+}, V^{4+}, and V^{5+} species, respectively [30]. In the spectrum of fresh 10V-3Ce/Al, the V^{3+} peak is absent because this species is oxidized during calcination in air. As shown in Table 3, the reaction significantly changes the content of V^{5+} species (the active species of ODHP [31]) in the oxygen carriers. After 15 min of reaction, 20.88% of the V^{5+} was completely converted to V^{3+}. Figure 7d compares the Ce 3d XPS spectra before and after the 10V-3Ce/Al reaction. Note that O_{latt} exists in CeO_2 [28]. As shown in Table 4, the Ce^{4+} content decreased from 63.27% before the reaction to 54.96% after the reaction; concomitantly, the Ce^{3+} content increased from 36.73% to 45.04% after the reaction. As the O_{latt} are slowly released, Ce^{4+} is not completely transformed into Ce^{3+}. The slow release of O_{latt} accompanies the valence change in the Ce and V elements. The whole reaction is an oxidation-reduction process, in which the O_{latt} released by the oxygen carrier catalyzes the oxidation of propane to propylene.

Table 3. Valence changes in the V element before and after the 10V-3Ce/Al reaction.

The Valence State of Element V	V^{5+}	V^{4+}	V^{3+}
Before reaction	41.92%	58.08%	0
After Reaction	21.04%	37.76%	41.20

Table 4. Valence changes in the Ce element before and after the 10V-3Ce/Al reaction.

The Valence State of Element Ce	Ce^{4+}	Ce^{3+}
Before reaction	63.27%	36.73%
After reaction	54.96%	45.04%

3. CL-ODHP Performance of the Oxygen Carrier

3.1. In Situ DRIFT Investigation of the 10V-3Ce/Al Oxygen Carrier

To further elucidate the catalytic oxidation mechanism, the 10V-3Ce/Al oxygen carrier was subjected to in situ DRIFT experiments in an N_2:C_3H_8 (v/v = 45:5) atmosphere. The vibration peaks at 1355, 1412, 1662, 2963, and 3189 cm^{-1} in the DRIFT spectra (Figure 8) are assigned to C-H bond stretching, C=O bond stretching, C=C bond stretching, variant Ce-O-V bonds, and V-OH bond stretching, respectively [7]. The peak at 1662 cm^{-1} is the absorption peak of CO_2 [7]. Note that the area under the C=C bond peak is smaller at 600 °C than at 550 °C, indicating that more olefins are generated at 550 °C than at 600 °C. V^{5+} is the main activation site of the C-H bond, and in the presence of V^{5+}, the propylidene C-H bond is broken and the propyl radical C_3H_7* and the hydrogen radical H* are adsorbed on the surface of the oxygen carrier [26]. When the temperature reaches 600 °C, the CO_2 peak is significantly enhanced. At high temperatures (600 °C), the inhibition of Ce^{4+} is weakened, the rate of O_{latt} evolution to O_{elec} is enhanced, and the propyl radical C_3H_7* is deeply oxidized to CO_x, while the high temperature (600 °C) weakens the metal-to-metal interaction forces, leading to the disruption of the V-O-Ce bond [20,32]. For this reason, the activity of the oxygen carrier was tested at 550 °C in this study.

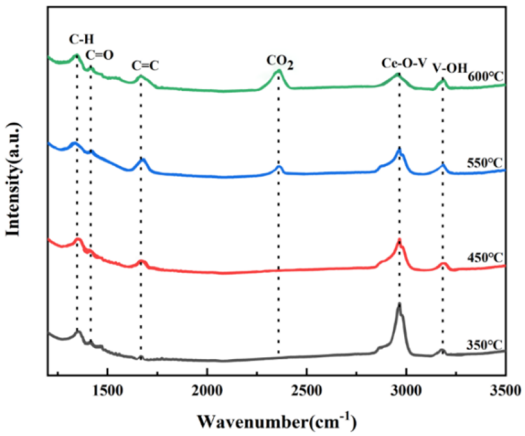

Figure 8. In situ diffuse-reflectance infrared Fourier-transform spectra of the 10V-3Ce/Al oxygen carrier at different temperatures (350–600 °C).

3.2. Effect of the Oxygen Carrier on Propane Conversion and Propylene Selectivity

Figure 9a compares the propane conversions of the 10V-XCe/Al oxygen carriers (X = 0, 1, 3, 5, 7). As CL-ODHP consumes O_{latt} from the oxygen carriers, the propane conversion decreases with increasing reaction time. The average propane conversion rates of 10V/Al, 10V-1Ce/Al, 10V-3Ce/Al, 10V-5Ce/Al, and 10V-7Ce/Al are 16.32%, 18.64%, 24.72%, 20.31%, and 23.16%, respectively, in the time range of 3-15 min. The results show that introducing CeO_2 at 550 °C significantly improves propane conversion. Propane conversion is maximized at a Ce loading of 3 wt.%. This improvement can be explained by oxygen loading in the oxygen carrier combined with a structural pore change. Ce increases the oxygen carrying capacity of the oxygen carrier; in particular, Ce^{4+} inhibits the conversion and loss of O_{latt} and facilitates the oxidation of propane to propylene [17]. In addition, a small amount of Ce increases the specific surface area of the oxygen carrier, exposing more active sites on the surface of the oxygen carrier. The propane then reacts more fully.

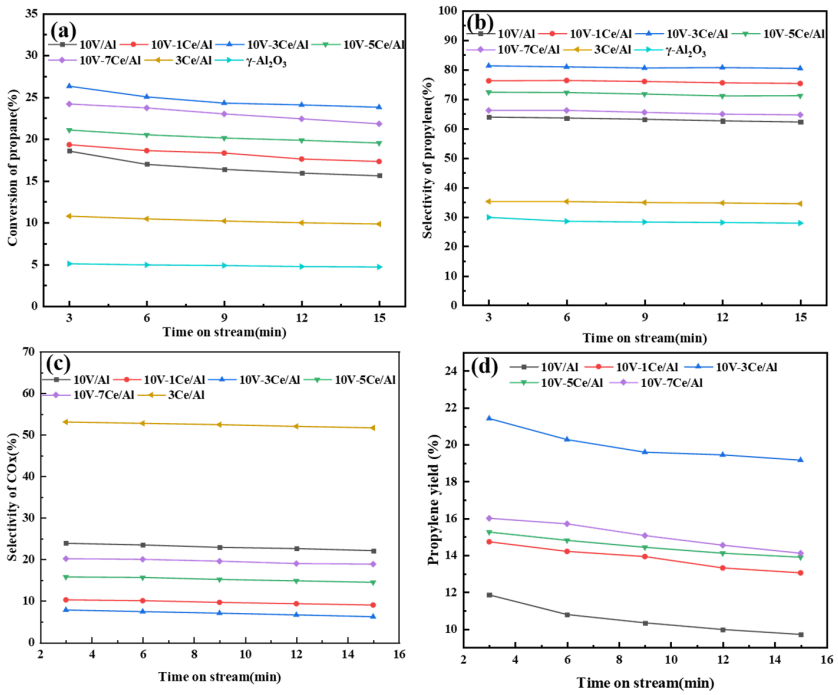

Figure 9. Effects of reaction time on (**a**) propane conversions, (**b**) propylene selectivity, (**c**) CO_x selectivity of the oxygen carriers, and (**d**) propylene yield.

Figure 9b compares the propylene selectivity of the 10V-XCe/Al oxygen carriers (X = 0, 1, 3, 5, 7). The propylene selectivity slowly decreases with increasing reaction time and is maximized at 83.42% at a Ce loading of 3 wt.%. The surface of the oxygen carrier hosts two main types of reactive oxygen species: O_{elec}, which oxidizes propane or propylene to CO_x by depth, and O_{latt}, which mainly reacts to produce propylene [33]. Previous XPS characterization showed that 10V-3Ce/Al contains more Ce^{4+} than the other samples. As Ce^{4+} inhibits the conversion of O_{latt} to O_{elec}, the 10V-3Ce/Al oxygen carrier retains a large number of O_{latt} and thus produces more propylene per unit time than the other oxygen carriers.

Figure 9c compares the CO_x selectivity of the 10V-XCe/Al oxygen carriers (X = 0, 1, 3, 5, 7). The 10V/Al oxygen carrier exhibits the highest CO_x selectivity (23.01%): the average CO_x selectivity values of 10V-1Ce/Al, 10V-3Ce/Al, 10V-5Ce/Al, 10V-7Ce/Al, and 3Ce/Al are 9.71%, 7.06%, 15.22%, 19.56%, and 52.42%, respectively. When the 3Ce/Al catalyst carrier (which lacks the VO_x component) reacts with propane, the O_{latt} species rapidly evolves into O_{elec} and propane is directly and deeply oxidized to CO_x, basically bypassing the ODHP effect [34].

Figure 9d compares the propylene yield of the 10V-XCe/Al oxygen carriers (X = 0, 1, 3, 5, 7). The average yields of propylene for 10V/Al, 10V-1Ce/Al, 10V-3Ce/Al, 10V-5Ce/Al, and 10V-7Ce/Al were 10.53%, 13.89%, 19.36%, 14.78%, and 15.23%. The propylene yield of 10V-3Ce/Al was improved by 83.86% compared to 10V/Al oxygenate carrier. From BET, it is known that 10V-3Ce/Al has the largest specific surface area, which provides more active for sites for CL-ODHP and facilitates the adequate reaction of propane. From H_2-TPR, 10V-3Ce/Al has the lowest reducibility. According to XPS, 10V-3Ce/Al has the highest O_{latt} capacity and Ce^{4+} content. Ce^{4+} inhibits the evolution of O_{latt} on the surface of the oxygen carrier towards O_{elec}, weakening the rate of propane being deeply oxidized to CO_x. Therefore, the average yield of propylene from 10V-3Ce/Al oxygen carriers is the highest.

3.3. CL-ODHP Cycling of the 10V/Al and 10V-3Ce/Al Oxygen Carriers

In this experiment, two oxygen carriers, 10V/Al and 10V-3Ce/Al, were cycled through 15 reaction regenerations at 550 °C. After 15 cycles, the propane conversion, propylene selectivity, and CO_x selectivity of the 10V-3Ce/Al oxygen carrier were 22.41%, 81.74%, and 6.88%, respectively (Figure 10), almost unchanged from those of the first dehydrogenation. The cyclic oxidative-dehydrogenation results confirmed the high reactivity and stability of the 10V-3Ce/Al oxygen carrier.

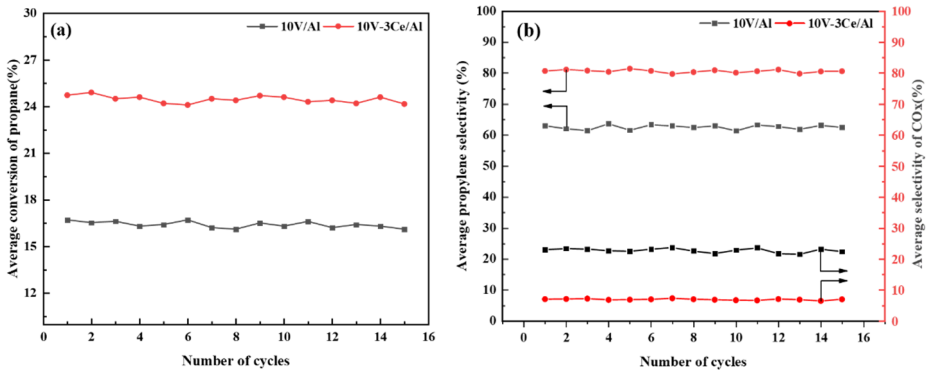

Figure 10. Effects of oxygen carrier cycling on (**a**) propane conversions and (**b**) propylene selectivity and CO_x selectivity of 10V/Al (black) and 10V-3Ce/Al (red).

Figure 11a XRD patterns of fresh oxygen carriers, Figure 11b XRD patterns of oxygen carriers after 15 cycles of CL-ODHP. No diffraction peaks of VO_x species were observed before and after the cycle, and the absence of VO_x species peaks could be due to the formation of highly dispersed amorphous VO_x phases or the formation of VO_x microcrystals undetectable by XRD [16]. The peak intensity of the CeO_2 phase of the 10V-3Ce/Al oxygen

carrier did not decrease significantly after cycling, indicating that the CeO_2 phase was still stably dispersed on the surface of the oxygen carrier after 15 cycles of CL-ODHP.

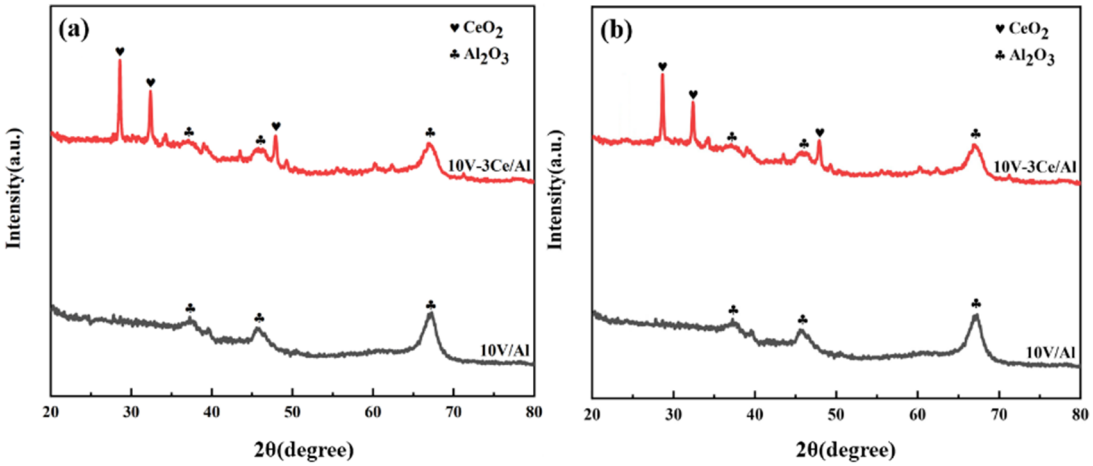

Figure 11. XRD spectra of (**a**) fresh 10V/Al and 10V10V-3Ce/Al 3Ce/Al oxygen carrier, (**b**) 10V/Al and 10V-3Ce/Al oxygen carrier after 15 CL-ODHP cycles.

Figure 12 shows the TEM of the 10V10V-3Ce/Al 3Ce/Al oxygenate before and after cycling. After 15 cycles of CL-ODHP, there is no sintering on the surface of the 10V-3Ce/Al oxygenate, indicating that the 10V10V-3Ce/Al 3Ce/Al oxygenates have good cycling stability. The lattice stripe spacing d = 0.31 nm corresponds to the (111) crystal plane of CeO_2. The lattice stripe spacing d = 0.28 nm corresponds to the (301) crystal planes of V_2O_5. V_2O_5 phase and CeO_2 phase are stable distributions on the surface of the oxygen carrier, indicating that the 10V-3Ce/Al oxygen carrier has good cycle stability.

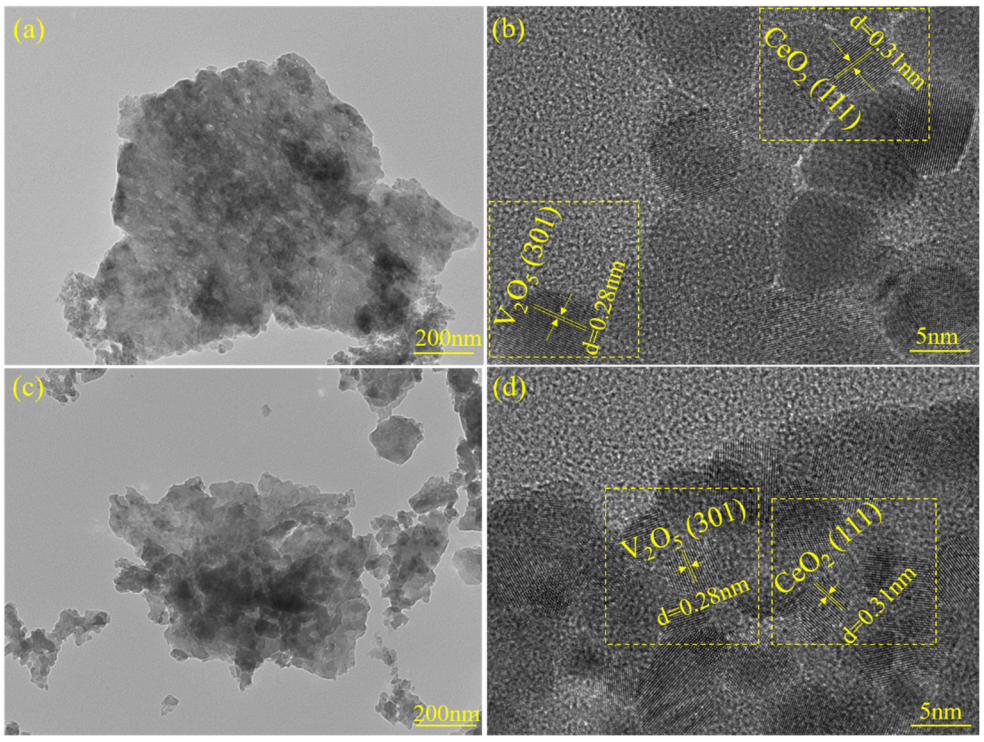

Figure 12. TEM images of (**a**,**b**) fresh 10V-3Ce/Al oxygen carrier, (**c**,**d**) 10V-3Ce/Al oxygen carrier after 15 CL-ODHP cycles.

4. Mechanism of CL-ODHP

The CL-ODHP follows the Mars-van Krevelen mechanism. The CL-ODHP mechanism was proposed by combining in situ DRIFT and XPS characterization. As shown in Figure 13, the first step of CL-ODHP is the adsorption of propane on the surface of the 10V-3Ce/Al oxygen carrier and the breaking of the propane methylene C-H bond. V^{5+} is the dehydrogenation activation site [16]. The rate-limiting step is breakage of the C-H bond of propane to form the propyl radical C_3H_7* and the hydrogen radical H*. Based on changes in XPS O_{latt} content before and after oxygen carrier reaction combined with previous in situ DRIFTS characterization, VO_x then releases O_{latt} to selectively oxidize C_3H_7* and H* to C_3H_6 and H_2O, respectively. CeO_2 uniformly dispersed on the surface of the oxygen carrier and controls the release and evolution rate of O_{latt}, thus avoiding the deep oxidation of C_3H_7*. However, at high temperatures (600 °C), CeO_2 loses its inhibition ability and O_{latt} rapidly evolves into O_{elec}, enabling the deep oxidation of C_3H_7* to CO_2 [20]. Similar results were obtained by Gong et al. and Zuo et al. Gong et al. [7] investigated the application of VO_x-TiO_2 oxygen carriers in CL-ODHP. V^{5+} is the main C-H bond activation site, and the propyl radical C_3H_7* and the hydrogen radical H* are generated by the breakage of the propane methylene bond under the activation of V^{5+}. Zuo et al. [20] investigated the application of CeO_2-modified 17.5 Cr/Al oxygen carriers in CL-ODHP. CeO_2 increased the amount of O_{latt} and enhanced the adsorption of propyl radicals, while Ce^{4+} modulated the rate of O_{latt} evolution to O_{elec} and propyl radicals were further oxidized to propylene.

Figure 13. Mechanism of CL-ODHP on the 10V-3Ce/Al oxygen carrier.

5. Experiment

5.1. Preparation of the Oxygen Carriers

Ce $(NO_3)\cdot 6H_2O$, NH_4VO_3, and $H_2C_2O_4\cdot 2H_2O$ were purchased from Sinopharm Group Chemical Reagent Co., Ltd., (Shanghai, China). Ce $(NO_3)\cdot 6H_2O$, NH_4VO_3, and $H_2C_2O_4\cdot 2H_2O$ were weighed and simultaneously dissolved in deionized water. During this process, the Ce content was adjusted to 0, 1, 3, 5, or 7 wt.%, and the mass ratio of oxalic acid to ammonium metavanadate was fixed at 2:1. The solution was then ultrasonicated for 30 min to ensure complete mixing of the constituents. After immersing the γ-Al_2O_3 carrier, the solution was allowed to stand at room temperature for 12 h and then dried in an oven at 90 °C for 12 h. The dried oxygen carrier was calcined in a 600 °C muffle furnace for 4 h (heating rate: 3 °C/min). Finally, the oxygen carrier was ground and sieved. The prepared samples were expressed as 10V-XCe/Al (VO_x content = 10 wt.%; CeO_y content, X = 0, 1, 3, 5, and 7 wt.%).

5.2. Oxygen-Carrier Performance Tests

Figure 14 shows the CL-ODHP reactor for investigating the activities of the oxygen carriers. The mass of the oxygen carriers was 0.50 g. The temperature was increased to 550 °C at 10 °C/min in an N_2 atmosphere. The N_2 was then purged for 20 min before passing propane through the reactor. The flow rates of the N_2 and C_3H_8 feed gases were 45 and 5 mL/min, respectively. After 3 min of reaction, the reaction gas was collected from the bottom of the quartz tube into a gas-sampling bag and then pumped into a gas

chromatograph (A91 Plus Panna, Guangzhou Baiwei Instrument Technology Co., Ltd., Guangzhou, China) for analysis.

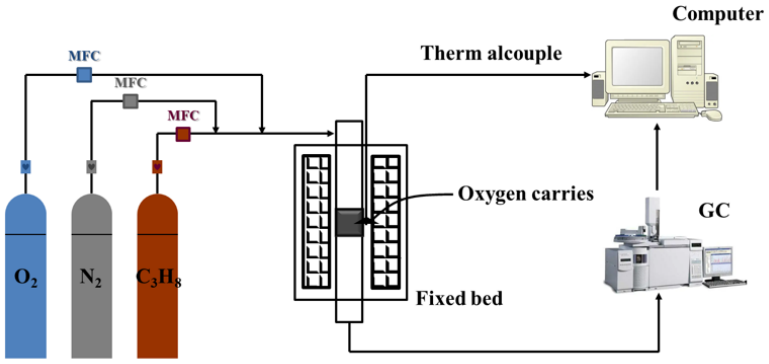

Figure 14. Schematic of the CL-ODHP setup.

The propane conversion, propylene selectivity, CO_x selectivity, and propylene yield were respectively calculated as follows:

Propane conversion rate

$$X_{C_3H_8} = \frac{N_{C_3H_6} + \frac{2}{3}N_{C_2} + \frac{1}{3}N_{C_1}}{N_{C_3} + \frac{2}{3}N_{C_2} + \frac{1}{3}N_{C_1}} \times 100\% \quad (1)$$

Propylene selectivity

$$S_{C_3H_6} = \frac{N_{C_3H_6}}{N_{C_3H_6} + \frac{2}{3}N_{C_2} + \frac{1}{3}N_{C_1}} \times 100\% \quad (2)$$

CO_x selectivity

$$S_{CO_x} = \frac{N_{CO_x}}{N_{C_3H_6} + \frac{2}{3}N_{C_2} + \frac{1}{3}N_{C_1}} \times 100\% \quad (3)$$

Propylene yield

$$Y_{C_3H_6} = X_{C_3H_8} \times S_{C_3H_6} \quad (4)$$

here, N represents the molar concentration of each substance at the outlet, C_1 denotes CH_4, CO, and CO_2, C_2 denotes C_2H_4 and C_2H_6, and C_3 denotes C_3H_6 and C_3H_8.

5.3. Oxygen Carrier Characterization

The structural and physical phases in the oxygen carrier were analyzed via X-ray diffraction (XRD) using a DX-2007 Advance X-ray diffractometer (Haoyuan Corporation, Dandong, China) with Cu Kα as the X-ray emission source, a tube voltage of 40 KV, and a wide angle-scanning range (5–90° in 5° increments). The structural parameters of the oxygen carriers were characterized using a Micromeritics TriStar 3000 physisorption instrument (Norcross, GA, USA) and the specific surface areas and pore-size distributions were calculated via Brunauer-Emmett-Teller and Barrett-Joyner-Halenda computational modeling, respectively. The sample to be tested was first degassed at 200 °C under vacuum for 3 h. The surface morphological characteristics of the oxygen carriers were observed under a scanning electron microscope (SEM) (JSM-IT100; JOEL Corporation, Tokyo, Japan) operated at 20 kV.

H_2 temperature-programmed reduction (H_2-TPR) was tested with a Micromeritics Autochen 2920 chemisorption instrument (Mack Corporation, USA). For this test, 50 mg of the sample was weighed and treated in a He atmosphere at 200 °C for 1 h. The treated sample was cooled to room temperature and the atmosphere was switched to 8% H_2/Ar, then purged until stabilization was achieved. After stabilization, the sample was heated to 900 °C and the H_2-TPR curve was obtained by recording the hydrogen consumption signal

with a thermal conductivity detector (TCD). The elemental valence states of the oxygen carriers were characterized using X-ray electron spectroscopy (XPS) (Kratos Analytical, Manchester, UK) with monochromatic AlKα ($h\nu$ = 1486.65 eV) as the excitation source. The sample to be tested was pressed and pretreated under the reaction conditions before loading it into the test bag. The thermal stabilities of the oxygen carriers were analyzed via thermogravimetric analysis (TGA) using an STA-409PC instrument (Netz, Selb, Germany) under an N_2 atmosphere. The temperature was increased from the programmed 30 °C to 800 °C and the tail-gas concentration was detected using TCD.

In situ diffuse-reflectance infrared Fourier-transform spectroscopy (DRIFTS) data were collected using a DRIFTS instrument equipped with a mercury-cadmium-telluride detector and an in situ reaction cell (Thermo Fisher Nicolet, Waltham, MA, USA). The resolution of the data collection was 4 cm^{-1}. Prior to analysis, the samples were dried at 600 °C for 30 min under an N_2 (45 mL/min) atmosphere. The background spectra were then collected at the required temperature while the temperature of the in situ reaction tank naturally declined to 30 °C. Subsequently, the oxygen carrier absorbed N_2: C_3H_8 (v/v = 45/5) gas mixture for 20 min. During measurements, the temperature was ramped at 3 °C/min. Each temperature point was stabilized for 10 min.

6. Conclusions

In this study, a series of 10V-XCe/Al oxygen carriers (X = 0, 1, 3, 5, 7) for CL-ODHP was prepared through an impregnation technique. The effects of Ce content on the catalytic activity and physicochemical properties of 10V-XCe/Al were investigated. The main findings are summarized below.

- Introducing CeO_2 increases the O_{latt} capacity of VO_x/γ-Al_2O_3 oxygen carriers and prolongs their catalytic oxidation activity. A certain amount of CeO_2 is uniformly dispersed on the surface of VO_x/γ-Al_2O_3 oxygen carriers, inhibiting the migration of O_{latt} species to electrophilic oxygen species, thus improving propylene selectivity.
- Among the prepared samples, 10V-3Ce/Al exhibits the highest specific surface area, the highest oxygen capacity, and the lowest reducibility. The 10V-3Ce/Al oxygen carrier also delivers the highest oxidative dehydrogenation performance.
- In the VO_x/γ-Al_2O_3 oxygen carrier with the CeO_2 additive (10V-3Ce/Al), the propylene selectivity improves to 83.42% (from 62.59% in 10V/Al) and the CO_x selectivity reduces to 6.88% (from 22.76% in 10V/Al).

Author Contributions: Conceptualization, F.Q.; data curation, F.Q.; formal analysis, F.Q., M.W. and T.G.; investigation, F.Q. and Q.G.; methodology, F.Q., T.G. and M.W.; software, F.Q. and M.N.; validation, F.Q., Q.G. and M.W.; visualization, F.Q., T.G., M.N. and Y.L.; writing—original draft, F.Q.; writing—review & editing, F.Q., T.G., Q.G. and M.W.; project administration, Q.G.; resources, Q.G.; supervision, Q.G. All authors have read and agreed to the published version of the manuscript.

Funding: This work was supported by the Joint Funds of the National Natural Science Foundation of China (U20A20124), Shandong provincial natural science foundation (ZR2020MB144), the State Key Laboratory of High-Efficiency Utilization of Coal and Green Chemical Engineering (2022-K3), and the Natural Science Foundation Project of Ningxia (2022AAC01001).

Data Availability Statement: Data sharing is not applicable to this article.

Acknowledgments: Thanks is expressed for the platform provided by Qingdao University of Science and Technology.

Conflicts of Interest: The authors declare no conflict of interest.

References

1. Chen, S.; Chang, X.; Sun, G.; Zhang, T.; Xu, Y.; Wang, Y.; Pei, C.; Gong, J. Propane dehydrogenation: Oxygen carrier development, new chemistry, and emerging technologies. *Chem. Soc. Rev.* **2021**, *50*, 3315–3354. [CrossRef]
2. Monai, M.; Gambino, M.; Wannakao, S.; Weckhuysen, B.M. Propane to olefins tandem catalysis: A selective route towards light olefins production. *Chem. Soc. Rev.* **2021**, *50*, 11503–11529. [CrossRef]

3. Dai, Y.; Gao, X.; Wang, Q.; Wan, X.; Zhou, C.; Yang, Y. Recent progress in heterogeneous metal and metal oxide oxygen carriers for direct dehydrogenation of ethane and propane. *Chem. Soc. Rev.* **2021**, *50*, 5590–5630. [CrossRef] [PubMed]
4. Hu, Z.P.; Yang, D.; Wang, Z.; Yuan, Z.H. State-of-the-art oxygen carriers for direct dehydrogenation of propane to propylene. *Chin. J. Catal.* **2019**, *40*, 1233–1254. [CrossRef]
5. Jiang, X.; Sharma, L.; Fung, V.; Park, S.; Jones, C.; Sumpter, B.; Baltrusaitis, J.; Wu, L. Oxidative dehydrogenation of propane to propylene with soft oxidants via heterogeneous catalysis. *ACS Catal.* **2021**, *11*, 2182–2234. [CrossRef]
6. Li, H.; Zhang, J.; Wu, P.; Xun, S.; Jiang, W.; Zhang, M.; Zhu, W.; Li, H. O_2 activation and oxidative dehydrogenation of propane on hexagonal boron nitride: Mechanism revisited. *J. Phys. Chem. C* **2019**, *123*, 2256–2266. [CrossRef]
7. Chen, S.; Pei, C.; Chang, X.; Zhao, Z.; Mu, R.; Xu, Y.; Gong, J. Coverage-Dependent Behaviors of Vanadium Oxides for Chemical Looping Oxidative Dehydrogenation. *Angew. Chem. Int. Ed.* **2020**, *59*, 22072–22079. [CrossRef]
8. Chen, S.; Zeng, L.; Mu, R.; Xiong, C.; Zhao, Z.; Zhao, C.; Pei, C.; Peng, L.; Luo, J.; Fan, L.; et al. Modulating Lattice Oxygen in Dual-Functional Mo-V-O Mixed Oxides for Chemical Looping Oxidative Dehydrogenation. *J. Am. Chem. Soc.* **2019**, *141*, 18653–18657. [CrossRef] [PubMed]
9. Liu, J.; Li, F. Mixed oxides as multi-functional reaction media for chemical looping catalysis. *Chem. Commun.* **2022**, *59*, 10–28. [CrossRef]
10. Wu, T.W.; Yu, Q.B.; Roghair, I.; Wang, K.; Annaland, M.S. Chemical looping oxidative dehydrogenation of propane: A comparative study of Ga-based, Mo-based, V-based oxygen carriers. *Chem. Eng. Process.* **2020**, *157*, 1076–1085. [CrossRef]
11. Jiang, X.; Zhang, X.; Purdy, S.C.; He, Y.; Huang, Z.; You, R.; Wei, Z.; Meyer, H.M.; Yang, J.; Pan, Y.; et al. Multiple promotional effects of vanadium oxide on boron nitride for oxidative dehydrogenation of propane. *JACS Au* **2022**, *2*, 1096–1104. [CrossRef]
12. Wang, J.; Wan, C.; Cheng, D.; Chen, F.; Zhang, X. Unveiling the morphology dependence of ceria nanocrystals for boosting low-temperature cyclohexane oxidative dehydrogenation. *Appl. Surf. Sci.* **2021**, *565*, 15060–15071. [CrossRef]
13. Prathap, C.; Ramana, K.V.V.; Venkata, R.M.; Nagaiah, P.; David, R.B. Promotional role of ceria in $CeO_2/MgAl_2O_4$ spinel oxygen carriers in CO_2 assisted selective oxidative dehydrogenation of ethylbenzene to styrene. *J. Ind. Eng. Chem.* **2019**, *79*, 97–105.
14. Wang, H.; Tsilomelekis, G. Catalytic performance and stability of Fe-doped CeO_2 in propane oxidative dehydrogenation using carbon dioxide as an oxidant. *Catal. Sci. Technol.* **2020**, *10*, 4362–4372. [CrossRef]
15. Shang, X.; Wang, X.; Nie, W.; Guo, X.; Zou, X.; Ding, W.; Lu, X. Facile strategy for synthesis of mesoporous crystalline γ-alumina by partially hydrolyzing aluminum nitrate solution. *J. Mater. Chem.* **2012**, *22*, 23806–23814. [CrossRef]
16. Khan, M.Y.; Adamu, S.; Lucky, R.A.; Hossain, M.M. Oxidative dehydrogenation of n-butane to C_4 olefins using lattice oxygen of VO_x/Ce-meso-Al_2O_3 under gas-phase oxygenfree conditions. *Energy Fuels* **2020**, *34*, 7410–7421. [CrossRef]
17. Liu, J.; Hao, M.; Chen, C.; Du, K.; Zhou, Q.; Zou, S.; Fan, J. Chlorinating CeO_2 at surface oxygen vacancies to promote their selectivity in oxidative dehydrogenation of propane to propene. *Appl. Surf. Sci.* **2020**, *528*, 147025. [CrossRef]
18. Kazerooni, H.; Towfighi Darian, J.; Mortazavi, Y.; Asadi, R. Titania-supported vanadium oxide synthesis by atomic layer deposition and its application for low-temperature oxidative dehydrogenation of propane. *Catal. Lett.* **2020**, *150*, 2807–2822. [CrossRef]
19. Fu, S.; Fang, Q.; Li, A.; Li, Z.; Han, J.; Dang, X.; Han, W. Accurate characterization of full pore size distribution of tight sandstones by low-temperature nitrogen gas adsorption and high-pressure mercury intrusion combination method. *Energy Sci. Eng.* **2020**, *9*, 80–100. [CrossRef]
20. Zuo, C.; Wu, M.; Guo, Q. The effect of the Ce content on the oxidative dehydrogenation of propane over CrO-CeO_2/γ-Al_2O_3 oxygen carriers. *Chin. J. Chem. Eng.* **2020**, *28*, 3035–3043. [CrossRef]
21. Nasution, P.S.; Jung, J.W.; Oh, K.; Koh, H.L. Coke combustion kinetics of spent Pt-Sn/Al_2O_3 oxygen carriers in propane dehydrogenation. *Korean J. Chem. Eng.* **2020**, *37*, 1490–1497. [CrossRef]
22. Xie, S.; Wang, Z.; Tan, W.; Zhu, Y.; Collier, S.; Ma, L.; Ehrlich, S.N.; Xu, P.; Yan, Y.; Xu, T.; et al. Highly Active and Stable Palladium Oxygen carriers on Novel Ceria-Alumina Supports for Efficient Oxidation of Carbon Monoxide and Hydrocarbons. *Environ. Sci. Technol.* **2021**, *55*, 7624–7633. [CrossRef]
23. Khan, M.Y.; Al-Ghamdi, S.; Razzak, S.A.; Hossain, M.M. Fluidized bed oxidative dehydrogenation of ethane to ethylene over VO_x/Ce-γAl_2O_3 catalysts: Reduction kinetics and catalyst activity. *Mol. Catal.* **2017**, *443*, 78–91. [CrossRef]
24. Hu, P.; Lang, W.Z.; Yan, X.; Chen, F.X.; Guo, Y.J. Vanadium-doped porous silica materials with high catalytic activity and stability for propane dehydrogenation reaction. *Appl. Catal. A-Gen.* **2018**, *553*, 65–73. [CrossRef]
25. Gu, J.; Zang, Y.; Gao, F. Study on preparation of vanadium oxide modified heteroatom B-Beta molecular sieve oxygen carrier and its catalytic performance on propane dehydrogenation. *J. Light Ind.* **2020**, *35*, 35–46.
26. Schumacher, L.; Hess, C. The active role of the support in propane ODH over VOx/CeO_2 oxygen carriers studied using multiple operando spectroscopies. *J. Catal.* **2021**, *398*, 29–43. [CrossRef]
27. Maslakov, K.I.; Teterin, Y.A.; Popel, A.J.; Teterin, A.Y.; Ivanov, K.E.; Kalmykov, S.N.; Petrov, V.G.; Farnan, I. XPS study of ion irradiated and unirradiated CeO_2 bulk and thin film samples. *Appl. Surf. Sci.* **2018**, *448*, 154–162. [CrossRef]
28. Kovacevic, M.; Agarwal, S.; Mojet, B.L.; Lefferts, L. The effects of morphology of cerium oxide oxygen carriers for dehydrogenation of ethylbenzene to styrene. *Appl. Catal. A Gen.* **2015**, *505*, 354–364. [CrossRef]
29. Shan, Y.; Zhao, W.; Zhao, S.; Wang, X.; Sun, H.; Yu, W.; Ding, J.; Feng, X.; Chen, D. Effects of alumina phases on the structure and performance of VOx/Al_2O_3 oxygen carriers in non-oxidative propane dehydrogenation. *Mol. Catal.* **2021**, *504*, 11466–11475.

30. Wang, Y.; Chen, S.; Sun, J.; Xie, Y.; Zhao, Z.; Gong, J. Roles of V-O sites for non-oxidative propane dehydrogenation over supported vanadium oxides. *Sci. China Mater.* **2022**, *603*, 1062–1070. [CrossRef]
31. Kaichev, V.V.; Chesalov, Y.A.; Saraev, A.A.; Tsapina, A.M. A Mechanistic study of dehydrogenation of propane over vanadia-titania oxygen carriers. *J. Phys. Chem. C* **2019**, *123*, 19668–19680. [CrossRef]
32. Huang, C.; Wang, Z.; Gong, X. Activity and selectivity of propane oxidative dehydrogenation over VO_3/CeO_2 (111) catalysts: A density functional theory study. *Chin. J. Catal.* **2018**, *39*, 1520–1526. [CrossRef]
33. Zeeshan, M.; Chang, Q.Y.; Zhang, J.; Hu, P.; Sui, Z.; Chen, D.; Zhu, Y. Effects of oxygen vacancy and Pt doping on the catalytic performance of CeO_2 in propane dehydrogenation: A first-principles study. *Chin. J. Chen.* **2021**, *39*, 2391–2402. [CrossRef]
34. Zuo, C.; Wu, M.; Guo, Q. CeO_2-CrOy-γ-Al_2O_3 redox oxygen carrier for the oxidative dehydrogenation of propane to propylene. *Can. J. Chem. Eng.* **2020**, *99*, 235–250. [CrossRef]